Research Square

Preprints are preliminary reports that have not undergone peer review.
They should not be considered conclusive, used to inform clinical practice,
or referenced by the media as validated information.

Ag/Al_2O_3/ITO memristor for honeybee-inspired associative learning, behavioral emulation, and conductance-constrained flower classification

Haoyu Li
Ningbo University
Jie Lu
Ningbo University
Junxiu Zhou
Ningbo University
Yun Wen
Ningbo University
Junyu Wang
Ningbo University
Xinyu Cao
Ningbo University
Weitian Xu
Ningbo University
Qiuyun Chen
Qingdao Tailao Technology Co., Ltd
Yegang Lu
Ningbo University
Ran Jiang
jiangran@nbu.edu.cn

Ningbo University

Research Article

Keywords: Al_2O_3 memristor, electrochemical metallization, synaptic plasticity, Pavlovian conditioning, conductance-state mapping

Posted Date: September 10th, 2026

DOI: https://doi.org/10.21203/rs.3.rs-10809143/v1

License: This work is licensed under a Creative Commons Attribution 4.0 International License.
Read Full License

Additional Declarations: No competing interests reported.

Ag/Al_2O_3/ITO memristor for honeybee-inspired associative learning, behavioral emulation, and conductance-constrained flower classification

Haoyu Li[a, §], Jie Lu[a, §], Junxiu Zhou[a], Yun Wen[a], Junyu Wang[a], Xinyu Cao[a], Weitian Xu[a], Qiuyun Chen[b], Yegang Lu[a], Ran Jiang[a, *]

[a] *School of Integrated Circuits, Ningbo University, Ningbo 315211, China*

[b] *Qingdao Tailao Technology Co., Ltd, Qingdao 266101, China*

[§] *Haoyu Li and Jie Lu contributed equally to this work.*

[*] *Corresponding author. Tel. +86 574 87600340; E-mail: jiangran@nbu.edu.cn*

Abstract: Honeybees identify floral cues and develop experience-dependent foraging behavior by associating odors with nectar rewards. Memristor conductance depends on prior stimulation and can be gradually tuned by electrical pulses, allowing changes in synaptic strength during learning to be represented electrically. Here, we fabricated an Ag/Al_2O_3/ITO memristor and examined how the compliance current and electrical pulses regulate its resistive-switching behavior and conductance states. Increasing the compliance current raised the low-resistance-state current while producing relatively little change in the high-resistance-state current, consistent with the progressive growth of an Ag conductive filament. Under pulsed stimulation, the device exhibited long-term potentiation and depression, paired-pulse facilitation, retention of well-separated resistance states for 10^3 s, and multilevel resistance modulation. Adjusting the pulse amplitude and sequence enabled the electrical emulation of Pavlovian conditioning, learning–forgetting–relearning, and graded states corresponding to sleep, drowsiness, and wakefulness. For flower classification, the weights of the CNN fully connected layer were mapped onto 50 discrete conductance states extracted from the experimentally measured LTP/LTD characteristics, whereas convolutional feature extraction remained in software. The conductance-mapped model achieved an accuracy of 86.55%, only 0.54 percentage points below the 87.09% obtained with the software model. These results show that different pulse protocols can produce distinct history-dependent responses within the same Ag/Al_2O_3/ITO device architecture, while the resulting device-derived conductance states can support device-constrained neural-network weight mapping.

Keywords: Al_2O_3 memristor; electrochemical metallization; synaptic plasticity; Pavlovian conditioning; conductance-state mapping.

Relevance Summary

1. Compliance-current-controlled Ag-filament growth tunes the resistance states of the Ag/Al_2O_3/ITO memristor; interfacial barriers and traps contribute to high-resistance transport.
2. Pulse-coded conductance modulation enables electrical emulation of synaptic plasticity, associative learning, and multiple honeybee-inspired behaviors.
3. Fifty measured memristor conductance states bridge device modulation and CNN flower classification, retaining 86.55% accuracy, only 0.54 points below software.

1 Introduction

Honeybees can discriminate floral cues such as color, shape, and odor in complex environments and associate these cues with nectar rewards, thereby adapting their foraging behavior through experience [1]. These capabilities depend on sensory information processing and activity-dependent modulation of synaptic strength, which together support learning and memory [2, 3]. Memristors exhibit a comparable form of history dependence: their conductance states depend on prior electrical stimulation and can be incrementally tuned by voltage pulses, allowing conductance to represent synaptic weight [4-6]. This property has enabled the emulation of long-term potentiation, long-term depression, and paired-pulse facilitation, together with the realization of multilevel conductance states [7-10].

The application scope of memristive neuromorphic systems has expanded beyond basic synaptic emulation to include Pavlovian conditioning [11-13], learning–forgetting dynamics [9, 14], multisensory integration, and bioinspired recognition tasks [15-17]. For example, a bee-inspired multisensory spiking-neuron system has been reported to integrate humidity and visual information for flower-authenticity recognition [18]. Nevertheless, most existing studies remain focused on a single sensory modality, a specific synaptic function, or an isolated recognition task. The extent to which the same resistive-switching platform can separately support synaptic plasticity, behavior-related state responses, and conductance-mapped classification

remains comparatively underexplored [11, 14, 15, 18]. Tailoring history-dependent device responses through electrical-pulse protocols may therefore provide a practical route to realizing multiple learning and behavior-related functions without altering the device structure.

In this work, we fabricated an Ag/Al_2O_3/ITO memristor and investigated how the compliance current and electrical pulses regulate its conductance response. Pulse-dependent conductance changes were used to emulate synaptic plasticity, while different stimulus-encoding protocols were applied to electrically reproduce Pavlovian conditioning, learning–forgetting–relearning, and graded behavioral states. For flower classification, the convolutional feature extractor remained in software, whereas the weights of the fully connected layer were mapped onto discrete conductance states extracted from the measured LTP/LTD characteristics to evaluate the influence of device-constrained weight mapping. These experiments examine synaptic learning, behavioral-state emulation, and neural-network weight mapping within the same Ag/Al_2O_3/ITO device architecture under different electrical protocols.

2 Experimental methods

Device fabrication and electrical measurements were performed at room temperature. Commercial ITO-coated glass substrates were cleaned using a standard RCA procedure and dried with N_2, with the ITO layer serving as the bottom electrode. A 100-nm-thick Al_2O_3 resistive-switching layer was deposited onto the ITO by electron-beam evaporation under a base pressure below 1×10^{-5} Torr at a deposition rate of 0.04–0.05 Å s^{-1}. Subsequently, 100-nm-thick Ag top electrodes with a diameter of 200 μm were deposited through a stainless-steel shadow mask at a rate of 0.13 Å s^{-1}, forming vertically stacked Ag/Al_2O_3/ITO devices.

The cross-sectional structure of the device was examined by scanning electron microscopy (SEM), and the elemental distributions of Ag, Al, and Sn were analyzed by energy-dispersive x-ray spectroscopy (EDS). The surface chemical composition and chemical states of the Al_2O_3 film were characterized by x-ray photoelectron spectroscopy (XPS). Electrical measurements were performed using a Primarius FS-Pro semiconductor parameter analyzer. Voltage was applied to the Ag top electrode, while the ITO bottom electrode was grounded.

3 Results and discussion

3.1 Device structure and material characterization

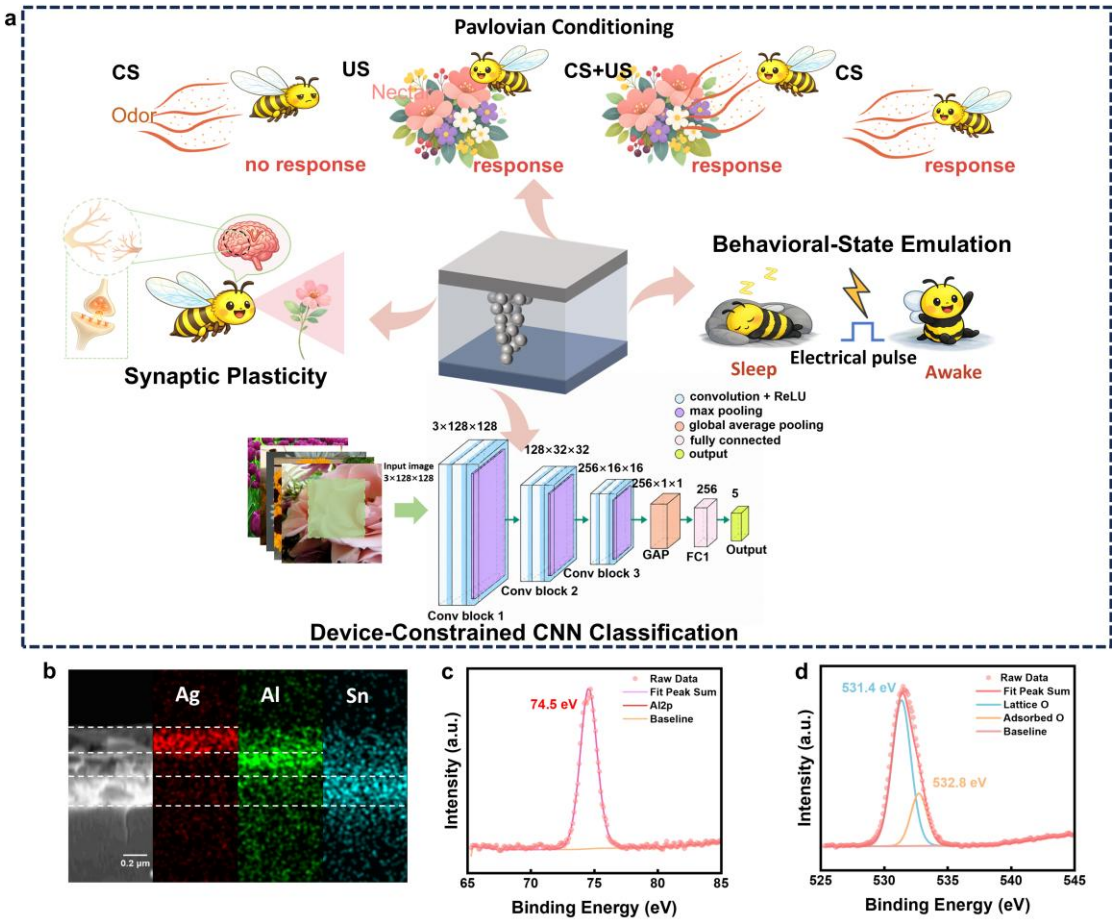


Fig. 1 (a) Schematic illustration of honeybee-inspired learning and behavioral-state emulation, together with a device-constrained CNN simulation for flower-image classification. (b) Cross-sectional SEM image and EDS elemental mappings of the Ag/Al_2O_3/ITO device. XPS measurements of the Al_2O_3 film: (c) Al 2p and (d) O 1s.

Fig. 1(a) schematically illustrates the honeybee-inspired functions investigated in this work, including memristor-based associative learning and behavioral-state emulation, together with flower-image classification using a convolutional neural network (CNN) constrained by device-derived conductance states. Fig. 1(b) shows a cross-sectional SEM image of the device and the corresponding EDS elemental maps. The SEM image reveals a well-defined Ag/Al_2O_3/ITO layered structure. The Ag, Al, and Sn signals are predominantly distributed in the regions corresponding to the Ag top electrode, Al_2O_3 resistive-switching layer, and ITO bottom electrode,

respectively, consistent with the intended device architecture.

The surface chemical composition and chemical states of the Al_2O_3 film were examined by x-ray photoelectron spectroscopy (XPS). The Al 2p spectrum in Fig. 1(c) exhibits a peak centered at 74.5 eV, which is assigned to Al^{3+} in Al–O bonds, consistent with reported values for Al_2O_3[19, 20]. As shown in Fig. 1(d), the O 1s spectrum can be deconvoluted into two components centered at 531.4 and 532.8 eV. The dominant component at 531.4 eV is attributed to lattice oxygen in the Al–O framework, whereas the higher-binding-energy component at 532.8 eV is associated with surface hydroxyl groups and adsorbed oxygen-containing species [19, 20].

3.2 Resistive-switching behavior and conduction mechanism

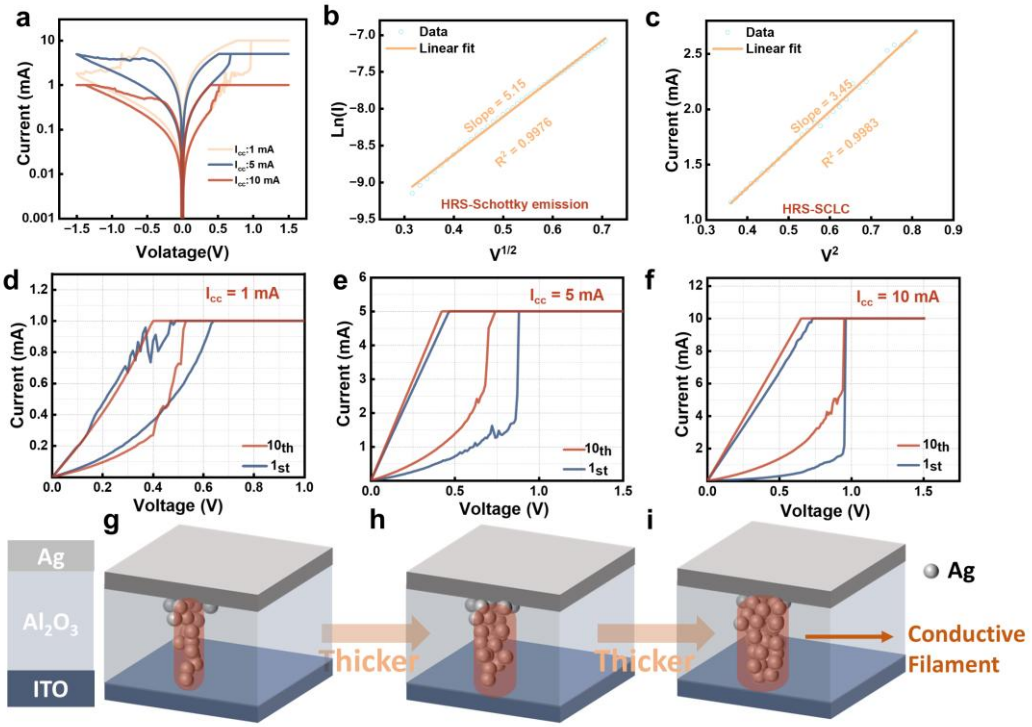


Fig. 2 Electrical characteristics and proposed conduction mechanism of the Ag/Al_2O_3/ITO memristor. (a) Bipolar I–V characteristics measured under compliance currents of 1, 5, and 10 mA. (b) Schottky-emission fitting and (c) space-charge-limited-conduction (SCLC) fitting of the high-resistance state. (d–f) First and tenth positive-voltage I–V sweeps selected from ten consecutive measurements at compliance currents of 1, 5, and 10 mA, respectively. (g–i) Schematic illustrations of the progressive formation and thickening of the Ag conductive filament with increasing compliance current.

To examine the effect of the compliance current (I_{CC}) on the resistive-switching behavior, the

I–V characteristics of the Ag/Al_2O_3/ITO memristor were measured at I_{CC} values of 1, 5, and 10 mA. As shown in Fig. 2(a), the LRS current progressively increases with increasing I_{CC}, whereas the HRS current exhibits comparatively limited variation. This behavior suggests that I_{CC} primarily regulates the development of the Ag conductive filament during the SET process, while exerting only a limited influence on HRS conduction [19, 21, 22].

To elucidate the carrier-transport behavior in the HRS, where a continuous Ag conductive filament is not expected to be fully established, the HRS I–V data were analyzed using established conduction models. In the low-voltage region, the approximately linear relationship between lnI and $V^{1/2}$ shown in Fig. 2(b) is consistent with Schottky emission associated with the electrode/Al_2O_3 interfacial barrier. With increasing voltage, the current exhibits an approximately linear dependence on V^2, as shown in Fig. 2(c), suggesting that space-charge-limited conduction (SCLC) becomes increasingly important under high electric fields. Taken together, the fitting results suggest that, before a continuous Ag conductive filament is established, the HRS transport may involve contributions from both the electrode/Al_2O_3 interfacial barrier and trap states within the Al_2O_3 layer [23, 24].

Figs. 2(d)–2(f) compare the first and tenth positive-voltage I–V sweeps selected from ten consecutive measurements at I_{CC} values of 1, 5, and 10 mA, respectively. At each I_{CC}, the two sweeps reach comparable compliance-limited LRS current levels, although some variation in the SET voltage is evident. The LRS resistance evaluated at 0.1 V decreases with increasing I_{CC}, consistent with the formation of an Ag conductive filament with a larger effective cross-sectional area at higher compliance currents.

A plausible physical mechanism is schematically illustrated in Figs. 2(g)–2(i). Under a positive bias, Ag atoms in the top electrode are oxidized to Ag^+ ions, which migrate through the Al_2O_3 resistive-switching layer under the applied electric field and are subsequently reduced and deposited near the ITO bottom electrode, gradually forming an Ag conductive filament across the functional layer [19, 21, 22]. At a low I_{CC}, the current is limited immediately after the SET transition, resulting in a relatively slender filament and, therefore, a higher LRS resistance. As I_{CC} increases, additional Ag^+ ions migrate and are reduced, leading to further filament thickening, reduced channel resistance, and an increased LRS current. Under a reverse bias, local dissolution and rupture of the filament are expected to occur preferentially at a constricted region, thereby

returning the device to the HRS. These results suggest that the LRS can be tuned through the compliance-current-controlled development of the Ag conductive filament.

3.3 Synaptic plasticity and biomimetic behaviors

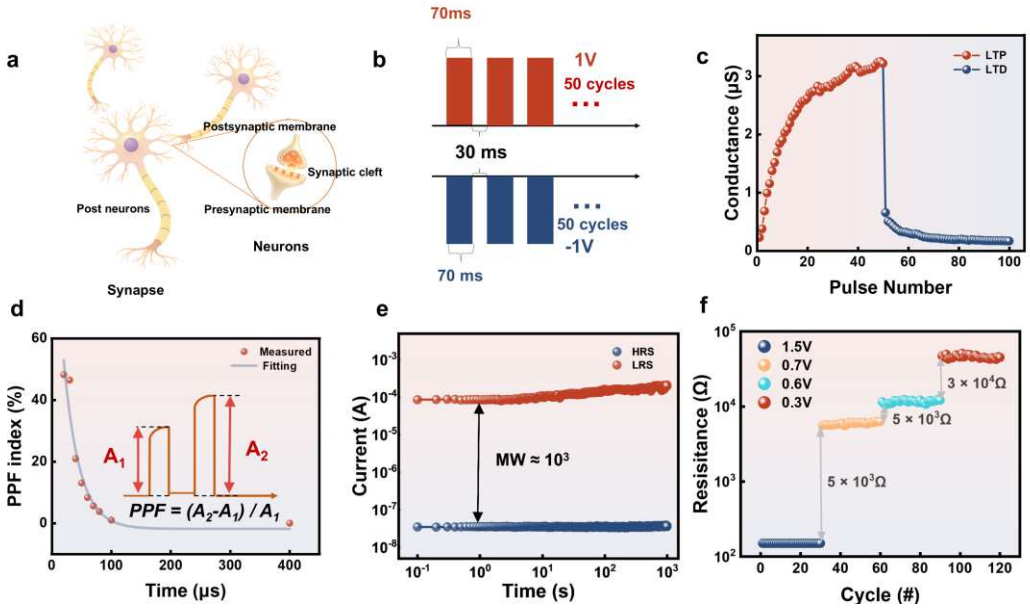


Fig. 3 (a) Schematic of a biological neuron and synapse. (b) Pulse protocol for LTP/LTD measurements. (c) Conductance modulation under 50 +1 V and 50 −1 V pulses with a width of 70 ms and an interval of 30 ms. (d) PPF index as a function of pulse interval. (e) Retention of the HRS and LRS. (f) Multilevel resistance states programmed by different pulse amplitudes.

Honeybees can learn and retain odor–reward associations through activity-dependent changes in synaptic strength [2]. As illustrated in Fig. 3(a), memristor conductance can serve as an analog of biological synaptic weight and can be gradually tuned by electrical pulses [6-8]. In the pulse protocol shown in Fig. 3(b), 50 potentiating pulses of +1 V and 50 depressing pulses of −1 V were applied, each with a width of 70 ms and an interval of 30 ms. As shown in Fig. 3(c), the device conductance gradually increases under positive pulses and subsequently decreases under negative pulses, emulating long-term potentiation (LTP) and long-term depression (LTD), respectively. This bidirectional conductance modulation corresponds to the strengthening and weakening of synaptic connections during learning [3].

The device also exhibits paired-pulse facilitation (PPF) [7, 25]. As shown in Fig. 3(d), the response amplitude induced by the second pulse (A_2) exceeds that induced by the first pulse (A_1). The PPF index is defined as

$$PPF=\frac{A_2-A_1}{A_1}\times 100\% \quad (1)$$

The PPF index decreases with increasing pulse interval, consistent with the temporal decay of short-term facilitation. The HRS and LRS remain clearly separated over 10^3 s, with a memory window of approximately 10^3 [Fig. 3(e)]. Multiple distinguishable resistance states can also be programmed by varying the pulse amplitude [Fig. 3(f)]. Together, these results demonstrate short-term facilitation, bidirectional long-term synaptic plasticity, HRS/LRS retention, and multilevel resistance programming, providing a device-level basis for the subsequent emulation of honeybee-inspired learning, memory, and behavioral states.

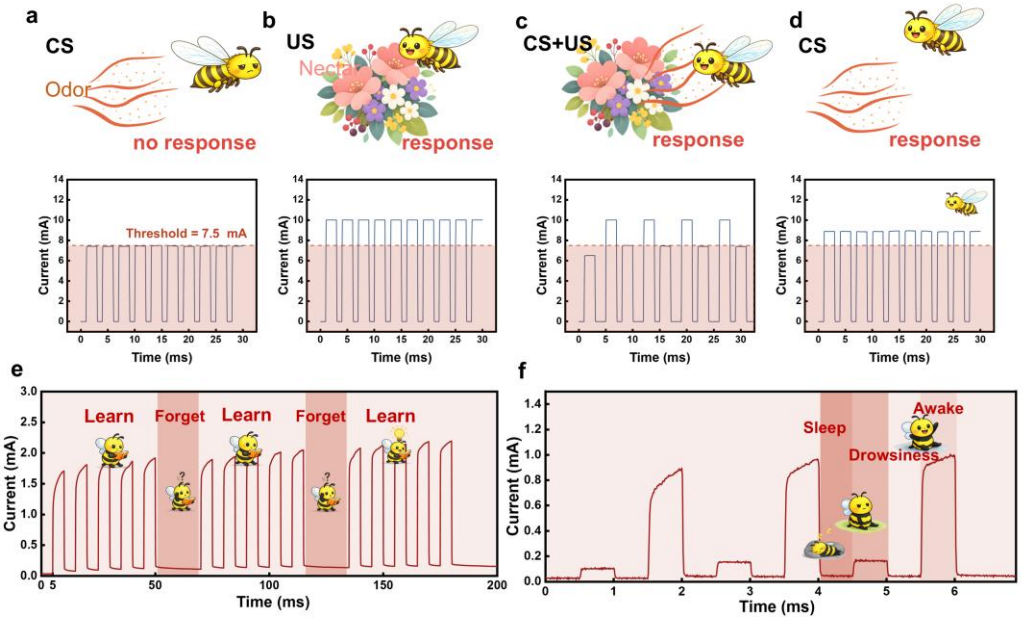


Fig. 4 (a–d) Electrical emulation of Pavlovian conditioning: (a) application of the 0.4 V conditioned stimulus (CS) before conditioning, producing an output current below the 7.5 mA response threshold; (b) application of the 0.6 V unconditioned stimulus (US), producing an above-threshold unconditioned response; (c) paired application of the CS and US for conditioning, resulting in an enhanced output response; and (d) application of the 0.4 V CS alone after

conditioning, producing an above-threshold conditioned response. (e) Dynamic current response during learning–forgetting–relearning cycles under 0.8 V training pulses, showing current decay after stimulus removal and an enhanced response during relearning. (f) Graded current responses induced by 0.1, 0.3, and 0.8 V pulses, mapped onto sleep, drowsy, and awake states, respectively.

The electrical emulation of Pavlovian conditioning is illustrated in Figs. 4(a)–4(d)[11-13]. Odor and nectar reward are encoded as pulse sequences with amplitudes of 0.4 and 0.6 V, respectively, and designated as the conditioned stimulus (CS) and unconditioned stimulus (US). An output-current threshold of 7.5 mA is used to distinguish between response and no-response states. Before conditioning, the 0.4 V CS pulses produce an output current below the threshold, corresponding to no response [Fig. 4(a)]. In contrast, the 0.6 V US pulses generate an above-threshold current, corresponding to an unconditioned response [Fig. 4(b)]. Paired application of the CS and US pulses increases the device conductance and output current, producing an above-threshold response [Fig. 4(c)]. After conditioning, reapplication of the 0.4 V CS pulses alone produces an output current above 7.5 mA [Fig. 4(d)]. The change in the CS-induced output from below the threshold before conditioning to above the threshold after conditioning represents the formation of a conditioned response.

The history-dependent response of the device also enables the emulation of learning–forgetting–relearning behavior[9, 14]. As shown in Fig. 4(e), 0.8 V training pulses are applied during the initial learning and relearning stages. Repeated stimulation progressively increases the output current, whereas the current gradually decays after the stimulation is removed, representing forgetting. Reapplication of the same training pulses restores the high-current response. The higher current attained during relearning suggests that part of the conductance change induced during the initial learning stage is retained.

The graded current responses induced by 0.1, 0.3, and 0.8 V pulses are mapped onto states corresponding to sleep, drowsiness, and wakefulness, respectively [Fig. 4(f)]. The low-current response induced by the 0.1 V pulses is mapped to sleep, the intermediate-current response induced by the 0.3 V pulses to drowsiness, and the high-current response induced by the 0.8 V pulses to wakefulness. Thus, varying the pulse amplitude enables the encoding of graded

behavior-related states. Together, these results show that tailored pulse protocols enable the Ag/Al_2O_3/ITO device platform to separately emulate associative learning, temporal learning dynamics, and graded behavior-related states through history-dependent conductance modulation.

3.4 Device-constrained flower classification

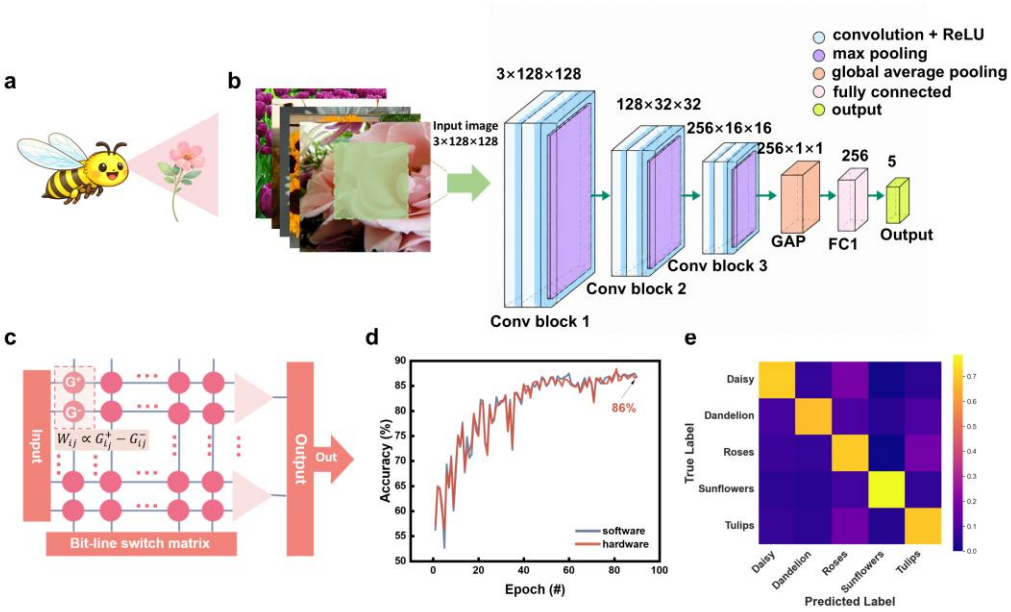


Fig. 5 (a) Schematic of honeybee-inspired flower vision. (b) Five-class flower dataset and CNN architecture. (c) Differential-conductance weight-mapping scheme. (d) Validation accuracies of the floating-point and conductance-mapped inference paths during software training and conductance-aware fine-tuning. (e) Normalized confusion matrix for five-class flower classification.

Bees distinguish rewarding flowers using visual cues such as color, shape, and texture [1, 17]. Motivated by this visual discrimination process, conductance states extracted from the measured LTP/LTD characteristics of the Ag/Al_2O_3/ITO device were incorporated into a five-class flower-classification task, as illustrated in Fig. 5(a). The flower_photos dataset contains images of daisies, dandelions, roses, sunflowers, and tulips. After resizing to 128×128 pixels, the RGB images were processed by three convolutional blocks with 64, 128, and 256 output channels,

respectively [Fig. 5(b)][26]. Each block contains two convolutional layers with batch normalization and ReLU activation, followed by max pooling. The resulting feature maps were reduced to a 256-dimensional vector by global average pooling and classified through a 256-to-5 fully connected layer.

The device characteristics were introduced after software training. As shown in Fig. 5(c), the convolutional feature extractor remained in the software domain, whereas the weights of the final fully connected layer were mapped onto discrete conductance states extracted from the measured LTP/LTD characteristics of the Ag/Al_2O_3/ITO device. Because the device conductance is non-negative, each signed weight was represented by a differential conductance pair,

$$W_{ij} = \alpha\left(G_{ij}^{+} - G_{ij}^{-}\right) \tag{2}$$

where G_{ij}^{+} and G_{ij}^{-} were selected from a set of 50 discrete conductance states extracted from the measured LTP/LTD characteristics, and α scales the conductance difference to the weight range of the network [27-29]. The mapped differential conductances were subsequently used in the fully connected inference path, while the convolutional parameters were retained in floating-point form [30-32].

As shown in Fig. 5(d), the software model achieved a classification accuracy of 87.09%. After replacing the fully connected weights with their measured-conductance representations, the accuracy remained at 86.55%, corresponding to a reduction of only 0.54 percentage points. The normalized confusion matrix in Fig. 5(e) retains a pronounced diagonal distribution, with class-wise recalls ranging from 81.05% to 92.54%. The remaining errors occur mainly between daisies and dandelions and between roses and tulips, likely reflecting similarities in their visual features. The small difference between the two inference paths shows that the experimentally accessible conductance states preserve most of the classification performance. This conductance-mapped classification complements the separately demonstrated synaptic and behavioral emulations, highlighting the functional adaptability of the Ag/Al_2O_3/ITO platform.

4 Conclusions

In this work, an Ag/Al_2O_3/ITO memristor was fabricated and investigated as a device platform for honeybee-inspired learning, behavioral-state emulation, and conductance-mapped flower classification. The LRS current increased with increasing compliance current, consistent with the progressive development of an Ag conductive filament. Under pulsed stimulation, the device exhibited long-term potentiation and depression, paired-pulse facilitation, retention of the HRS and LRS over 10^3 s, and multilevel resistance modulation. By varying the pulse combinations and amplitudes, Pavlovian conditioning, learning–forgetting–relearning behavior, and graded states corresponding to sleep, drowsiness, and wakefulness were emulated using the same Ag/Al_2O_3/ITO device architecture. The weights of the fully connected layer in the flower-classification CNN were mapped onto 50 discrete conductance states extracted from the measured LTP/LTD characteristics. The classification accuracy changed from 87.09% for the software model to 86.55% after conductance mapping, corresponding to a decrease of 0.54 percentage points. These results demonstrate that the same Ag/Al_2O_3/ITO device structure can exhibit multiple history-dependent responses by modifying the applied pulse protocol, while the resulting device-derived conductance states provide a practical basis for device-constrained neural-network weight mapping.

Additional experimental and mapping details are provided in Online Resource 1, including the electrical measurement and HRS fitting procedure, Al_2O_3 surface topography, additional honeybee-inspired behavioral responses, the Pavlovian-conditioning pulse protocol, and the conductance states used for CNN weight mapping.

REFERENCES

[1] M.V. Srinivasan, Annu. Rev. Entomol. 55, 267 (2010). https://doi.org/10.1146/annurev.ento.010908.164537

[2] M. Giurfa, J.-C. Sandoz, Learn. Mem. 19, 54 (2012). https://doi.org/10.1101/lm.024711.111

[3] R. Malenka, M. Bear, Neuron 44, 5 (2004). https://doi.org/10.1016/j.neuron.2004.09.012

[4] R. Waser, M. Aono, Nat. Mater. 6, 833 (2007). https://doi.org/10.1038/nmat2023

[5] J.J. Yang, D.B. Strukov, D.R. Stewart, Nat. Nanotechnol. 8, 13 (2013). https://doi.org/10.1038/nnano.2012.240

[6] S.H. Jo, T. Chang, I. Ebong, B.B. Bhadviya, P. Mazumder, W. Lu, Nano Lett. 10, 1297 (2010). https://doi.org/10.1021/nl904092h

[7] Z. Wang, S. Joshi, S.E. Savel'ev, et al., Nat. Mater. 16, 101 (2017). https://doi.org/10.1038/nmat4756

[8] H. Bian, Y.Y. Goh, Y. Liu, H. Ling, L. Xie, X. Liu, Adv. Mater. 33, 2006469 (2021). https://doi.org/10.1002/adma.202006469
[9] B. Zhao, M. Xiao, Y.N. Zhou, Nanotechnology 30, 425202 (2019). https://doi.org/10.1088/1361-6528/ab3260
[10] I. Maity, R. Bharti, A.K. Mukherjee, A.D. Thakur, Appl. Phys. Lett. 126, 013504 (2025). https://doi.org/10.1063/5.0235922
[11] M. Ziegler, R. Soni, T. Patelczyk, et al., Adv. Funct. Mater. 22, 2744 (2012). https://doi.org/10.1002/adfm.201200244
[12] Z.-H. Tan, X.-B. Yin, R. Yang, S.-B. Mi, C.-L. Jia, X. Guo, Sci. Rep. 7, 713 (2017). https://doi.org/10.1038/s41598-017-00849-7
[13] A.K. Jena, M.C. Sahu, K.U. Mohanan, et al., ACS Appl. Mater. Interfaces 15, 3574 (2023). https://doi.org/10.1021/acsami.2c17228
[14] F. Shi, K. Wang, Y. Cao, J. Mou, Neural Netw. 195, 108291 (2026). https://doi.org/10.1016/j.neunet.2025.108291
[15] C. Jiang, H. Xu, W. Wang, et al., Device 3, 100897 (2025). https://doi.org/10.1016/j.device.2025.100897
[16] Y. Wang, Q. Zhang, Y. Li, et al., Appl. Phys. Rev. 12, 021328 (2025). https://doi.org/10.1063/5.0230234
[17] H. Lian, Z. Dou, Z. Qin, et al., Adv. Mater. 37, e2416649 (2025). https://doi.org/10.1002/adma.202416649
[18] K. Pan, C. Chen, X. Li, et al., Chem. Eng. J. 512, 162479 (2025). https://doi.org/10.1016/j.cej.2025.162479
[19] H. Du, F. Wang, Z. Li, et al., J. Phys. Chem. Lett. 16, 2722 (2025). https://doi.org/10.1021/acs.jpclett.5c00184
[20] J. van den Brand, W. Sloof, H. Terryn, J. de Wit, Surf. Interface Anal. 36, 81 (2004). https://doi.org/10.1002/sia.1653
[21] I. Valov, R. Waser, J.R. Jameson, M.N. Kozicki, Nanotechnology 22, 254003 (2011). https://doi.org/10.1088/0957-4484/22/25/254003
[22] M. Speckbacher, M. Rinderle, O. Bienek, I.D. Sharp, A. Gagliardi, M. Tornow, Nanoscale 16, 19675 (2024). https://doi.org/10.1039/d4nr02870h
[23] H. Spahr, S. Montzka, J. Reinker, F. Hirschberg, W. Kowalsky, H.-H. Johannes, J. Appl. Phys. 114, 183714 (2013). https://doi.org/10.1063/1.4829910
[24] L. Gao, Y. Li, Q. Li, Z. Song, F. Ma, Nanotechnology 28, 215201 (2017). https://doi.org/10.1088/1361-6528/aa6cd0
[25] R.S. Zucker, W.G. Regehr, Annu. Rev. Physiol. 64, 355 (2002). https://doi.org/10.1146/annurev.physiol.64.092501.114547
[26] Y. LeCun, Y. Bengio, G. Hinton, Nature 521, 436 (2015). https://doi.org/10.1038/nature14539
[27] M. Prezioso, F. Merrikh-Bayat, B.D. Hoskins, G.C. Adam, K.K. Likharev, D.B. Strukov, Nature 521, 61 (2015). https://doi.org/10.1038/nature14441
[28] M. Hu, C.E. Graves, C. Li, et al., Adv. Mater. 30, 1705914 (2018). https://doi.org/10.1002/adma.201705914
[29] P. Yao, H. Wu, B. Gao, et al., Nature 577, 641 (2020). https://doi.org/10.1038/s41586-020-1942-4

[30] H. Kang, H.W. Kim, E.R. Hong, J. Woo, Appl. Phys. Lett. 120, 122101 (2022). https://doi.org/10.1063/5.0086164
[31] Y. Zhang, Z. Wu, S. Liu, et al., Front. Neurosci. 15, 717222 (2021). https://doi.org/10.3389/fnins.2021.717222
[32] J. Jang, Y. Song, S. Park, Adv. Intell. Syst. 7, 2400710 (2025). https://doi.org/10.1002/aisy.202400710

Statements and Declarations

Funding

This work was funded by the Ningbo Municipal Science and Technology Innovation Yongjiang 2035 Key R&D Plan (Grant No. 2025Z086) and the Natural Science Foundation of Ningbo Municipality (Grant No. 2023J007). This work was also supported by the Graduate Student Scientific Research and Innovation Project of Ningbo University.

Competing Interests

The authors have no conflicts to disclose.

Author Contributions

Haoyu Li and Jie Lu: Conceptualization, Methodology, Investigation, Formal analysis, Data curation, Visualization, and Writing – original draft. Junxiu Zhou, Yun Wen, Junyu Wang, Xinyu Cao, and Weitian Xu: Investigation and Validation. Qiuyun Chen: Methodology and Writing – review & editing. Yegang Lu: Methodology, Supervision, and Writing – review & editing. Ran Jiang: Conceptualization, Supervision, Project administration, Funding acquisition, and Writing – review & editing. All authors reviewed and approved the final manuscript.

Data Availability

The data that support the findings of this study are available from the corresponding author upon reasonable request.

Supplementary Files

This is a list of supplementary files associated with this preprint. Click to download.

- ESM1JMSE.docx